

Cite this: *J. Mater. Chem.*, 2012, **22**, 15635

www.rsc.org/materials

PAPER

Interactions of nanoparticles with purple membrane films†

Jennifer M. Bulpett,^a Andrew M. Collins,^a Noor H. M. Kaus,^a Philip T. Cresswell,^a Oier Bikondoa,^{bc} Dominic Walsh,^a Stephen Mann,^a Sean A. Davis^a and Wuge H. Briscoe^{*a}

Received 19th April 2012, Accepted 21st June 2012

DOI: 10.1039/c2jm32467a

Lamellar structures self-assembled from purple membranes (PM) of *Halobacterium salinarum* are promising building units for bio-electronic devices, due to proton pumping ability of the PM. The functionality and durability of such devices are hinged on the structural integrity of PM lamellae. Using X-ray diffraction, we examined the structure of PM multilayers on silicon when challenged with two types of nanoparticles (NPs): carboxymethyl-dextran coated magnetite (2.4 nm core size) and citrate-stabilised gold (5 nm core size). We tried to infiltrate the PM multilayers with the NPs using two alternative routes: facile penetration (FP) and co-assembly (CS) by solution mixing. We found that under all conditions the NPs did not disrupt the overall lamellar structure of the PM films or enter the inter-lamellar space, although the presence of NPs affected the self-assembly process of the PM films. This caused an increase in the disorder in the film structure, as assessed by the decreasing number of layers in the multilayer stack as the NP concentration increased. Despite this, UV-Vis spectroscopic measurements showed that the conformation of the retinal residue within the protein was intact so the proton pumping functionality of PM multilayers would be retained in all samples with added NPs. Our results show that the effects of NPs on the PM structure and functionality are subtle and complex, and we will discuss the structural integrity of lipid-protein composite PM films against NP infiltration in terms of their high bending modulus as compared with that of fluid lipid bilayers.

1. Introduction

Using natural mechanisms for new technological applications has long been an inspiration for materials scientists and engineers. There are many examples in modern technological applications where the design and construction of novel nanocomposite materials with sophisticated structures¹ and functions have attempted to emulate the processes of biological living systems.² Products created in this way, for instance, include self-cleaning paint inspired by the lotus effect³ and quality control sensors based on the human nose.⁴ It is not surprising that the electronics industry has increasingly been looking towards natural systems to allow products to be more compact and efficient. Amongst the many possible ways of designing systems based on those naturally occurring is bio-inspired self-assembly exploiting either biologically originated molecules or their synthetic counterparts. Purple membranes (PMs) have been

shown to be promising building blocks for constructing electronic devices using such bio-inspired self-assembly mechanisms.

PM consists of 75% bacteriorhodopsin (bR) protein embedded in 25% lipid and is isolated from *Halobacterium salinarum* where it is found in patches on the cell wall.⁵ *H. salinarum* is an organism from the Archaea domain and can survive at extremely high salt concentrations due to its ability to act as a proton pump. The bR membrane protein has a molecular weight (MW) of 26 kDa and is made up of 248 amino acid residues arranged into seven α helices which span across the cell membrane.^{6,7} The bR proteins form a trimeric array to produce a 4.9 nm-thick single layer of hexagonally packed unit cells, 6.3 nm in size (*cf.* Fig. 1). Retinal, an enzyme within the bR protein, can absorb light, instigating a photocycle with numerous intermediates, which forces protons across the membrane creating a proton gradient, with protons being moved out of the cell,⁸ leading to suggestions of using PM in single-electron transistors⁹ and electrochemical devices with nano-electrodes.¹⁰ It has been shown that if multilayers of PM are formed, such proton-pumping effect can be amplified.^{11–13} Thus, a number of recent studies have focused on achieving such multilayer structures on surfaces, and also on the intercalation of acidic polymers in the inter-lamellar space which could further facilitate the pumping process by the conduction of protons between layers and reinforce the PM structure.^{8,14–16}

For these PM-derived electronic devices to function and be durable, it is important that the structural integrity of the

^aSchool of Chemistry, University of Bristol, Cantock's Close, Bristol BS8 1TS, UK. E-mail: wuge.briscoe@bristol.ac.uk

^bDepartment of Physics, University of Warwick, Gibbet Hill Road, Coventry, CV4 7AL, UK

^cXMaS, the UK-CRG Beamline, European Synchrotron Radiation Facility (ESRF), 6 Rue Jules Horowitz, B.P. 220, 38043 Grenoble, CEDEX 9, France

† Electronic supplementary information (ESI) available. See DOI: 10.1039/c2jm32467a

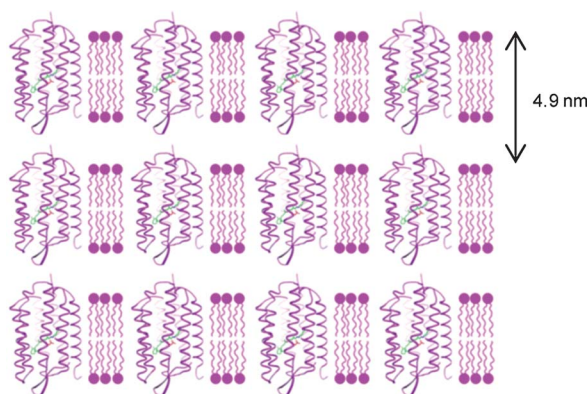


Fig. 1 Schematic representation of the purple membrane structure adapted from Collins *et al.*¹⁵

multilayer structure can withstand various challenges, mechanical or chemical, from the environment in which they are intended to function. PM has shown considerable resilience under moderate to severe chemical conditions. For example Collins *et al.*¹⁶ have successfully intercalated PM multilayers with aminopropyl-functionalised silica and shown that this increased the photovoltaic response of the films and resistance of the functional protein to degradation with solvents.

In another PM based study Collins *et al.*¹⁵ formed partially intercalated poly(methacrylate) PM films by adding methacrylic acid (MA) solution to a preformed PM film, and then subsequent crosslinking of MA with a reaction solution. This resulted in freestanding films which did not fragment like untreated PM films, and the PM films with crosslinked MA also withstood immersion in neutral aqueous suspension for 7 days in contrast to native PM films or PM films with un-crosslinked MA which would disperse. The films were also ethanol resistant and the lifetime of the deprotonated M-intermediate in the photochromic cycle was increased; a useful feature for design of optical storage devices.

Nanoparticles (NPs) have been increasingly used in many products, for instance, zinc oxide (ZnO) in piezo-electric sensors¹⁷ and titanium dioxide (TiO₂) in self-cleaning glass,¹⁸ and they are potentially useful in a number of electronic products. As such, the components of a bio-inorganic hybrid electronic device should be able to withstand NP exposure by design, but also, where possible, they should be robust to exposure by contamination from NPs in other products or during use. There have been a handful of studies exposing PM, and in some cases extracted bR protein, to NPs to try and modify the function of the proton pump, but these have not specifically examined how the structure of the PM film is affected and where the NPs are incorporated within the structure.

Recently, Yen *et al.*⁸ investigated whether bR could be used as part of an electrochemical cell. Citrate-stabilised silver (Ag), silver–gold (Ag–Au) alloy and gold (Au) NPs about 30 nm in diameter were mixed in solution with bR and the change in the surface plasmon resonance (SPR) was observed. The presence of NPs increased the photocurrent density as the surface plasmons of Au and Ag caused the rate of proton release to increase, speeding up the photocycle, with the Ag NPs having the largest observable effect. In that study it was shown that the addition of NPs to the bR increased its functionality and thus the

incorporation of NPs would have beneficial effects on devices (such as a solar cell) where the PM and NPs are in direct contact.

Another study where NPs and PM were in direct contact was carried out by Sumitomo *et al.*¹⁰ In that study a silicon substrate was overlaid with carbon nanotubes (CNTs) and the PM was deposited atop and viewed with an atomic force microscope (AFM) to establish whether the silicon–CNT substrate could improve the spatial resolution. The PM did not appear damaged, but whether its functionality was compromised by the CNTs was not examined.

In this study, we would like to evaluate the structural and functional integrity of PM multilayers against NPs. Two different NPs (carboxymethyl-dextran stabilised magnetite NPs (Fe₃O₄NPs) of 2.4 nm core size and citrate-stabilised AuNPs of 5 nm core size; *cf.* Fig. 2) were chosen, and their effects on PM films were probed. Both NPs have established biomedical applications: for instance, carboxymethyl-dextran stabilised Fe₃O₄NPs can be utilised in magnetic resonance imaging (MRI);¹⁹ AuNPs have many uses²⁰ including catalysis and as bio-sensors, and the enhancement of the bR function by citrate-stabilised AuNPs of a larger size (~30 nm) has been previously studied.⁸ The main motivation in our study, however, is to use these two types of NPs as model NPs for their size, and their differing surface chemistry and core type. The NPs were added to PM with two methods: *facile penetration (FP)* and *co-assembly (CS)*. A range of NP concentrations was utilised spanning over 4 orders of magnitude. The particular sizes of the NPs were chosen as smaller size NPs were thought to be more likely to intercalate into the PM multilayers. The structure of the resultant films was examined with X-ray diffraction performed in an X-ray

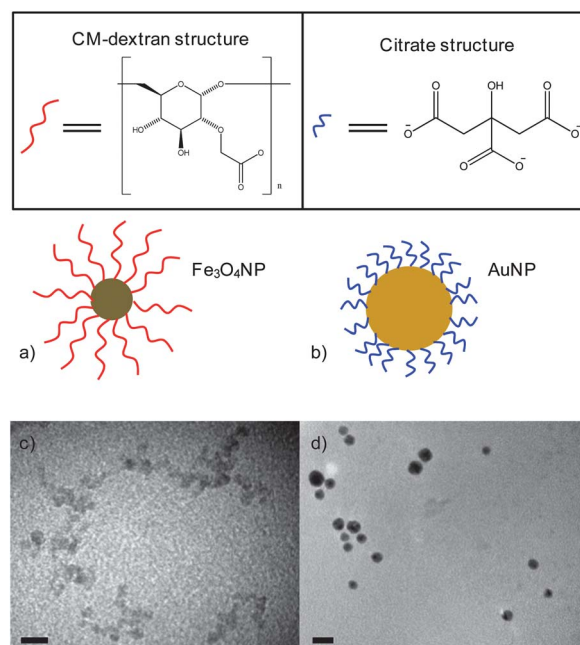


Fig. 2 Schematic drawing to show NPs with surface coating: (a) cm-dextran coated magnetite (2.4 nm core size, 91.3 nm hydrodynamic radius by DLS due to clustering), (b) citrate stabilised gold NPs (5 nm quoted core size (4.57 nm by TEM), 10.1 nm hydrodynamic radius by DLS), (c) TEM image of aggregated magnetite NPs, and (d) TEM image of dispersed gold NPs, scale bars are 10 nm. NP size histograms are provided in the ESI.†

reflectivity (XRR) configuration, their topography imaged with an AFM and their chemical functionality characterised with ultraviolet-visible (UV-Vis) absorption spectroscopy. We find that the overall structural integrity of the PM films was largely retained in all our samples with different NP concentrations and prepared with two different methods (*FP* and *CS*), although the PM films became less ordered as the NP concentration was increased. The conformation of retinal in all of the films was not affected by the presence of the NPs.

2. Experimental section

2.1. Materials

Wild type purple membrane (PM) was a gift from Norbert Hampp (University of Marburg) and purified using standard procedures as previously reported.²⁰ Stock PM suspensions were prepared by dispersion in MilliQ water (with a resistivity of 18.2 MΩ cm) at a concentration of 5.5 mg mL⁻¹. Magnetite nanoparticles (Fe₃O₄NPs), of 2.4 nm mean core diameter and coated with carboxymethyl-dextran biopolymer (MW ~ 15 000), were prepared according to a published procedure.^{21,22} Briefly an aqueous precipitation of mixed Fe³⁺/Fe²⁺ salts with strong base in the presence of the dissolved carboxymethyl-dextran was conducted. Bulk precipitate was removed by centrifugation and salts extracted by use of a size exclusion chromatography (SEC) column. Their mean core diameter was estimated from transmission electron microscopy (TEM) images as 2.4 nm (*cf.* Fig. 2(c)). They were dispersed in MilliQ water at a concentration of 5 mg mL⁻¹ and stirred for 2–3 hours to ensure complete dispersion before addition to PM films. Aqueous suspensions (0.0058 mg mL⁻¹) of gold nanoparticles (AuNPs) of 5 nm mean core diameter (*cf.* Fig. 2(b)) were purchased from Sigma-Aldrich®, containing <0.01% tannic acid, <0.04% sodium citrate and 0.02% sodium azide, and were used as received.

2 cm × 1 cm quartz pieces and silicon wafers purchased from University Wafers were used as substrates for PM films, and they were cleaned by sonication in a 1 : 1 ethanol : acetone mixture for 30 minutes. They were then left to dry in an oven at 40 °C overnight. The surfaces were carefully wiped with Bodyguards Hospitex medical wipes to remove any residue left by the solvent.

2.2. Sample preparation for XRR and AFM

Samples with six different number ratios ν (ref. 23) of NPs : PM trimer, ranging from 0.001 to 4.1 were investigated. A summary of the samples is listed in Table 1, together with the NP core diameters (D) and the method for NP addition (β). The samples are labelled as, *e.g.*, PM ν NP β , where ν is the number ratio, NP the nanoparticle core type and β (= *CS* or *FP*) the NP addition method. The corresponding volume ratios are also listed, estimated as $\nu_v = 4/3\pi(D/2)^3/(V_{\text{bR}} + V_{\text{lipids}})$, where the volume of the bR protein trimer $V_{\text{bR}} \sim 101.2 \text{ nm}^3$, and that of the associated lipids $V_{\text{lipids}} \sim 40.8 \text{ nm}^3$.²⁴

For “solution co-assembled” (*CS*) samples, 20 μL of 5.5 mg mL⁻¹ PM solution was mixed with 20 μL of gold or magnetite solution in varying concentrations. The solution was then deposited onto a piece of cleaned silicon and left for at least 5 hours to dry in an enclosed humidified box with a relative humidity of 65% as controlled by bubbling air through a saturated salt solution. For “facile-penetration” (*FP*) samples a piece of

cleaned silicon had 20 μL of PM solution added to its centre, spreading across the width of the piece. They were left to dry for 5 hours in a humidified box. After the films were dried, 20 μL of an aqueous NP solution was drop cast onto the silicon, covering the purple membrane film and again the films were left to dry in the humidified box. The samples for UV-Vis measurements were prepared similarly, using quartz as the substrate. Details of the samples are displayed in Table 1 (as well as their d -spacing, coherence length L and the number of layers m , to be discussed later). The overall PM film thickness for samples is estimated by scanning electron microscopy (SEM) to be ~10 to 20 μm .

2.3. Experimental techniques

X-ray diffraction (XRD) of the PM films was carried out at the XMaS UK CRG beamline (BM 28) at the European Synchrotron Radiation Facility (ESRF) in Grenoble, France. The monochromatic X-ray beam had an energy of 10 keV, corresponding to an X-ray wavelength $\lambda = 1.24 \text{ \AA}$, and the beam size was defined to 300 $\mu\text{m} \times 1000 \mu\text{m}$ (height \times width) by 2 sets of slits. The incident angle θ_i was varied in the range 0.06–2° for each of the measurements, corresponding to a momentum transfer $Q = 4\pi\sin\theta_i/\lambda$ range of 0.011–0.354 \AA^{-1} . The diffraction data were collected using an avalanche photodiode detector (APD) in the specular reflection plane but at angles with a small offset of 0.06° to the incident angle (*i.e.* $\theta_r = \theta_i \pm \Delta\theta$; ($\Delta\theta = 0.06^\circ$)) to minimise the contribution from the silicon substrate. PM samples on solid silicon substrates were mounted inside a small chamber enclosed with kapton films which allowed a constant flow of helium during the measurements to reduce background scattering. Each sample was checked for visible damage after sample alignment, and in addition, possible beam damage was avoided by making measurements on several fresh regions of the sample by moving the sample laterally perpendicular to the incident beam. XRD can be used to probe structures with Bragg peaks emerging when long range order occurs. PM has been viewed with XRD previously and Bragg peaks emerge as a result of the regularly spaced multilayers, giving a d spacing of 4.9 nm.²⁵

AFM imaging was carried out using a Veeco Picoforce with a high resolution tip (*i.e.* 1 or 2 nm tip radius) (Super-SharpSilicon™ cantilever from Nanosensors; spring constant 10–130 N m⁻¹ and resonant frequency 204–497 kHz) in tapping mode (TM) within a noise-proof box. Samples on both silicon and quartz were imaged, and the topography of the film was recorded as the tip scanned across the surface of the film.

UV-Vis absorption spectroscopy of PM films on quartz was performed using a PerkinElmer Lambda-35 instrument in the wavelength range 200–700 nm. The NP size was estimated from TEM images, taken with a JEOL Mk1 or Mk2, where the NPs in aqueous solution were deposited on 3 mm carbon coated copper grids. Dynamic light scattering (DLS) measurements of Fe₃O₄NPs and AuNPs in aqueous solutions were carried out using Malvern Instruments Zen1600 Zetasizer Nanoseries at 20 °C.

3. Results and discussion

3.1. PM film structure by X-ray diffraction (XRD)

XRD has been shown to be a powerful tool to obtain the structural information of surface PM multilayers in a previous study by

Table 1 Sample details including NP type, number ratio, volume ratio, preparation method, layer thickness, coherence length and corresponding number of layers

Sample	NP type	NP core diameter D (nm)	No. ratio ν NP : trimer	Vol. ratio ν_v NP : trimer	Prep. method β	Layer thickness d (nm)	Coherence length L (nm)	No. of layers m	$\lambda \sim 560$ nm UV-Vis absorption peak
PM	None		0.000	0	N/A	4.71 ± 0.01	71 ± 7.1	15.1 ± 0.1	Yes
PM 0.008 Fe ₃ O ₄ CS	Fe ₃ O ₄	2.4	0.008	0.000572	CS	4.66 ± 0.01	75 ± 7.5	16.1 ± 0.1	Yes
PM 0.08 Fe ₃ O ₄ CS	Fe ₃ O ₄	2.4	0.080	0.00572	CS	4.68 ± 0.01	61.1 ± 3.4	13.1 ± 0.7	Yes
PM 0.08 Fe ₃ O ₄ FP	Fe ₃ O ₄	2.4	0.080	0.00572	FP	4.67 ± 0.01	64.5 ± 6.5	13.8 ± 1.4	Yes
PM 0.8 Fe ₃ O ₄ CS	Fe ₃ O ₄	2.4	0.800	0.0572	CS	4.75 ± 0.05	38.7 ± 0.1^a	8.15 ± 0.1	Yes
PM 4.1 Fe ₃ O ₄ FP	Fe ₃ O ₄	2.4	4.091	0.293	FP	4.71 ± 0.06	40.2 ± 3.1	8.6 ± 0.7	Yes
PM 4.1 Fe ₃ O ₄ CS	Fe ₃ O ₄	2.4	4.083	0.293	CS	4.8 ± 0.01	29.4 ± 2.9	6.1 ± 0.1	Yes
PM 0.0008 Au CS	Au	5	0.001	0.000518	CS	4.68 ± 0.01	81 ± 8.1	17.3 ± 0.1	Yes
PM 0.008 Au CS	Au	5	0.008	0.00518	CS	4.73 ± 0.01	76.6 ± 7.7	16.2 ± 0.1	Yes
PM 0.008 Au FP	Au	5	0.008	0.00518	FP	4.65 ± 0.03	70.4 ± 14.3	15.2 ± 3.2	Yes
PM 0.08 Au CS	Au	5	0.080	0.0518	CS	4.68 ± 0.03	72.6 ± 7.6	15.5 ± 1.7	Yes
PM 0.2 Au FP	Au	5	0.206	0.129	FP	4.87 ± 0.01	36.9 ± 3.7	7.6 ± 0.1	Yes
PM 0.2 Au CS	Au	5	0.206	0.129	CS	N/A	N/A	N/A	Yes

^a Where more than one position on a sample was viewed, the values for coherence length *etc.* have been averaged and the standard deviation is shown.

Koltover *et al.*²⁵ Fig. 3 shows the relative reflectivity curves *vs.* Q for all the co-assembled (CS) PM films with both gold (Au) and magnetite (Fe₃O₄) NPs at different number ratios ν . To obtain the relative reflectivity, the reflection data were normalised with the maximum intensity, and the curves in the figure are offset on the vertical scale for clarity. The curve for the control PM sample without any added NPs is shown as the purple curve A, which displays two characteristic peaks, as indicated by two dark arrows in the figure, at $Q_1 = 0.133 \text{ \AA}^{-1}$ and $Q_2 = 0.265 \text{ \AA}^{-1}$. The ratio of these two peak positions, $Q_1 : Q_2 = 1 : 2$, indicates that these are Bragg diffraction peaks of order $n = 1$ and 2 arising from a lamellar structure, with a d -spacing of $d = 2\pi/Q_1 = 4.72 \text{ nm}$. All the PM films with NPs added with the CS method in Fig. 3 (Fe₃O₄NPs, curves B – E; AuNPs, curves F, G and H) showed such diffraction peaks, and this is also true for the films prepared with the facile penetration (FP) method as shown in Fig. 4, indicating that the overall lamellar structure was retained for all the PM films with added NPs. We can evaluate the d -spacing (or the thickness of each PM layer in the multilayer structure) for all the films by examining the peak Q positions. A change in the d -spacing would manifest as a shift of the Bragg peaks to a different Q value. We have observed such slight shifts to smaller Q values with added NPs (*e.g.* comparing curve E in Fig. 4 with the control curve A in the figure), suggesting an increase in the d -spacing or the layer thickness due to NP addition. In Table 1, we list the d -spacing for all the PM films, and we plot d *vs.* the number ratio ν for PM films with Fe₃O₄NPs in Fig. 5(a) and with AuNPs in Fig. 6(a) (■ in the figures; left vertical axes for d). It can be concluded that, although the d -spacing of the PM films was not significantly altered with an average value of $4.73 \pm 0.05 \text{ nm}$ for the two types of NPs added and for different NP concentrations, there is a trend for a slight increase in the d -spacing as ν is increased (*i.e.* with more NPs added). However, the increase in the d -spacing is very small, with the maximum value $\Delta d \sim 0.16 \text{ nm}$, which is insufficient to accommodate AuNPs or Fe₃O₄NPs in the inter-lamellar spacing, or a full monolayer of water molecules (0.275 nm in size). We suggest that it may be due to cations (*e.g.* Na⁺, $\sim 0.1 \text{ nm}$ in size; Fe³⁺, $\sim 0.064 \text{ nm}$ in size²⁶) from NPs binding to the bR protein residues which expose –COOH terminus. Some of these available

binding sites have been reported to locate on the extracellular side of the bR protein (*e.g.* Glu-74 residue²⁷), *i.e.* on the surface of the PM layer, and others are embedded in the interior of the bR protein. As we will discuss later in light of our UV-Vis results, it is

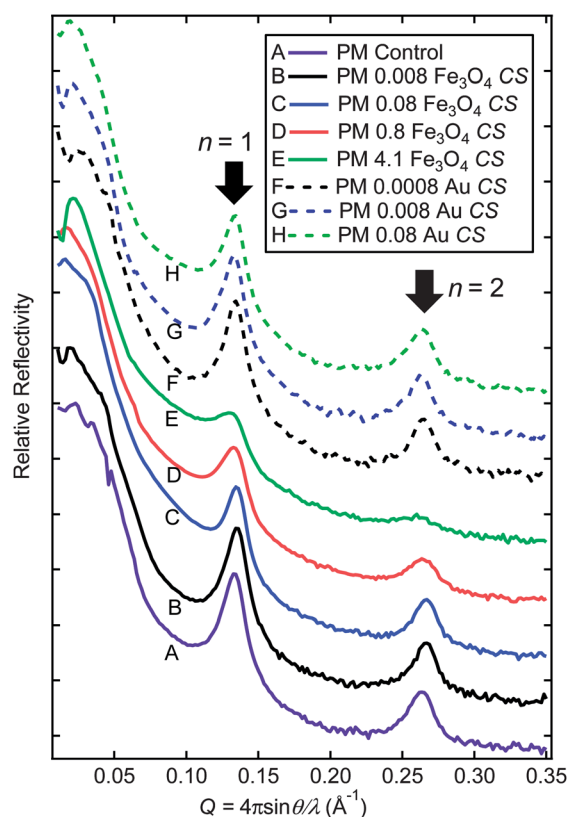


Fig. 3 Relative reflectivity *vs.* Q for all the co-assembled (CS) PM films with both Fe₃O₄NPs (solid curves B – E) and AuNPs (dashed curves F – H) with that for the PM control sample (no NPs added) shown as the purple curve A. The two dark downward arrows point to two diffraction peaks corresponding to orders $n = 1$ and 2 respectively, which gives a d -spacing for the PM lamellae as $\sim 4.73 \pm 0.05 \text{ nm}$.

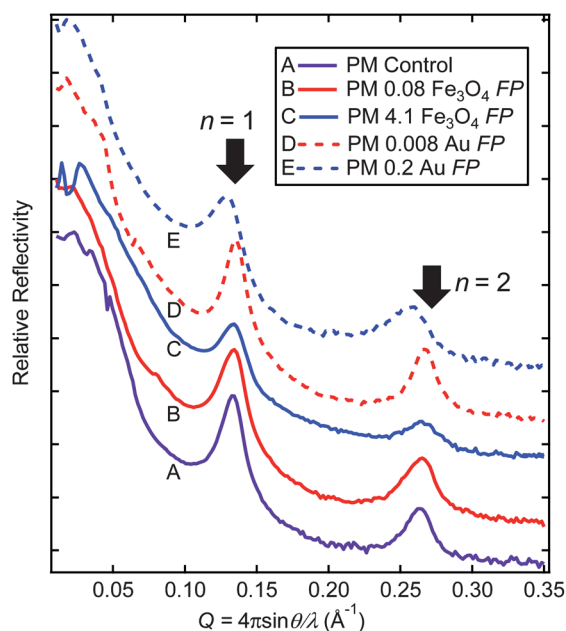


Fig. 4 Relative reflectivity vs. Q for all the facile penetrated (FP) PM films with both AuNPs and Fe_3O_4 NPs with that for the PM control sample (no NPs added) shown as the purple curve A. The two dark arrows point to two diffraction peaks corresponding to orders $n = 1$ and 2 respectively. All the films retained a d -spacing for the PM lamellae $\sim 4.73 \pm 0.05$ nm, except for the sample with the highest AuNP number ratio $\nu = 0.2$, whose Bragg peaks shift to a smaller Q value, giving $d = 4.88$ nm.

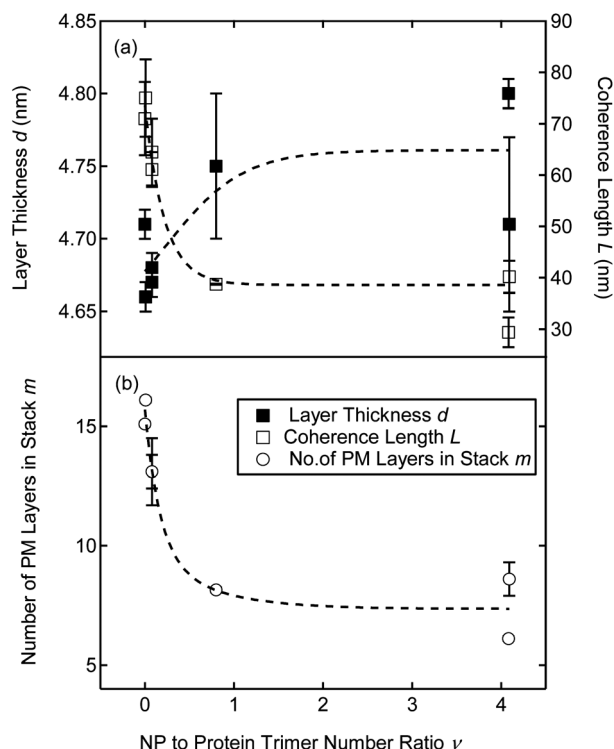


Fig. 5 (a) The PM layer thickness d (■; left axis) and the coherence length L (□; right axis) in PM films with Fe_3O_4 NPs, plotted against the NP to PM trimer number ratio ν and (b) the number of PM layers m in each multilayer stack (○) vs. ν for Fe_3O_4 NPs added to the PM films using both CS and FP methods. The dashed curves are a guide for the eye.

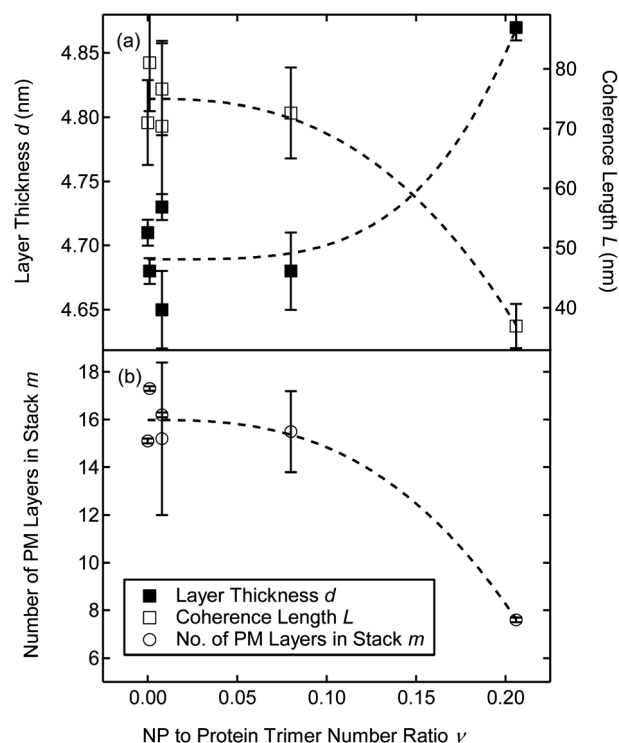


Fig. 6 (a) The PM layer thickness d (■; left axis) and the coherence length L in PM films (□; right axis) plotted against the AuNP to PM trimer number ratio ν , and (b) the number of PM layers m in each multilayer stack (○) vs. ν for AuNPs added to the PM films using both CS and FP methods. The dashed curves are a guide for the eye.

most likely that the cations were trapped interstitially, probably as hydrated ions. This in turn will increase the fluidity and flexibility of the PM layers, leading to augmented undulation forces.²⁶ As such, the slight increase in the d -spacing should not be interpreted as due to a monolayer of trapped hydrated ions, but instead it is possibly related to the augmented undulation forces between the layers arising from their enhanced flexibility. The effect of the surface dextran coating of the NPs (as shown in Fig. 2) would no doubt dominate these interactions; however the details of this mechanism could not be identified in the literature and will require further experimental investigations.

In addition to the d -spacing calculated from the Bragg peak positions, we may also examine the shape or the broadening of the Bragg peaks, which will provide information on the size of the ordered domains in the film and in turn the number of lamellar PM layers in the multilayer stack and the overall long range order in the PM multilayer structure. Such peak broadening, especially evident in curve E in Fig. 3, may be assessed by its full width at half maximum (FWHM), ΔQ , and the domain size may be characterised by a coherence length L , related to each other by the Scherrer equation,^{28,29} $L = 2\pi K/\Delta Q$, where K is a shape factor of order unity. The coherence lengths L for all the PM films obtained from their first Bragg peaks are listed in Table 1, along with the number of PM layers $m = L/d$. In Fig. 5(a) and 6(a), we plot L vs. the number ratio ν for PM films with Fe_3O_4 NPs and AuNPs respectively (□ in the figures; right vertical axes for L), with the corresponding number of layers in the multilayer stack, m , plotted

in Fig. 5(b) and 6(b) respectively. These show a clear trend for an increase in L and a decrease in m with more NPs added, suggesting that the PM films became more disordered. This is consistent with our observation of d -spacing increase with NP addition. All the L and m values are also listed in Table 1.

In a paper by Koltover *et al.*,²⁵ XRR of PM films was carried out which yielded coherence lengths (L) on the order of over 300 nm, much larger than those presented in this paper, where $L \sim 71$ nm for our PM control sample. The lower coherence length for the samples examined in this work is most likely due to the drop-casting method of film formation, whereas Koltover fused the PM patches of around 1 μm into large 10 μm patches and then stacked these to create extremely well oriented multilayers. As L is an indication of the crystallinity of the samples it is unsurprising that the drop-casting method produced less ordered films.

The overriding feature of the XRD curves from all samples both with and without NPs is that they show similar features: the diffraction peaks are retained and the peak Q positions do not differ significantly, implying that the NP's presence, even at highest concentration, did not completely destroy the multilayered structure in all the PM films. This suggests that the structural integrity of the PM has prevented the NPs from significantly disrupting its layered structure. The two different methods also yielded similar results showing that either the NPs fail to invade the preformed PM films (in the case of *FP*) or are excluded as the PM multilayers dry down (in the case of *CS*).

However, more subtle effects on the structure of the PM films in the presence of NPs are evident from analysing the coherence lengths L and the exact layer thickness d . As Fig. 5(a) shows, in general as the concentration of Fe_3O_4 NPs increases, d increases and L decreases quite rapidly until the number ratio $\nu \sim 1$, and then the trend plateaus. This trend is confirmed in Fig. 5(b) in which the number of layers m in the PM multilayer stacks in the film shows a rapid decay with ν before stabilising at $\nu > 1$. Fig. 6(a) shows the effects of AuNP concentration on d and L , and again L decreases and d increases with increasing ν but no plateau is seen in Fig. 5(a). The number of layers in the multilayer stack, m , again decreases with increasing ν showing that with both NPs the crystallinity of the sample is affected by NP exposure, albeit not disrupted completely. These observations suggest that NPs have affected the self-assembly process of PM film formation, with fewer layers in the assembled multilayer stacks. We have tentatively interpreted this as a result of increased flexibility of, and in turn increased repulsive undulation forces between the PM layers due to binding of hydrated cations to bR amino acid residues. As such, the effect of NPs on the structure of PM films is indirect and subtle. An outstanding question is then, if the NPs are excluded from the inter-lamellar space, where do they reside? To shed light on this question, we have used AFM imaging to examine the topography of the obtained PM films, as described in the following section.

3.2. AFM topography of PM films

The topography of the PM films and NP distribution on the film surface were investigated by AFM imaging (Fig. 7). AFM has been used to visualise surface bound PM extensively.^{10,30} The morphology of the PM control film (Fig. 7(a)) shows an uneven and patchy surface, consistent with previous AFM images of

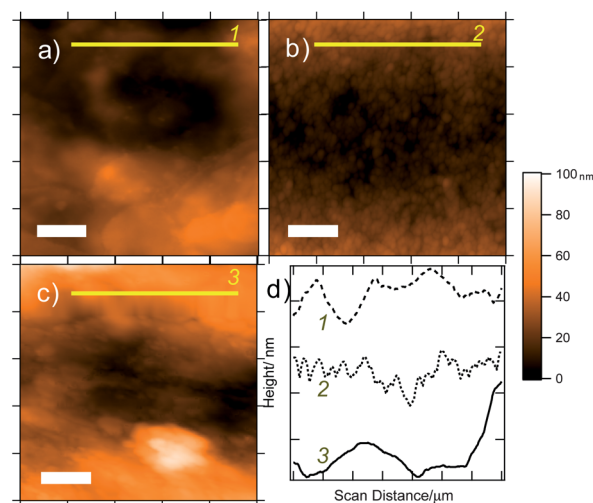


Fig. 7 AFM images of PM films showing location of line profiles, and all scale bars are 200 nm. (a) Control PM sample showing overlapping PM patches, RMS roughness ~ 6.52 nm; (b) [PM4.1 Fe_3O_4 FP], RMS roughness ~ 8.1 nm; (c) [PM0.2AuFP], RMS roughness ~ 17.58 nm; (d) line profiles of each sample.

similar films. The PM patches overlap with each other causing the undulating surface seen in the figure, and the outline of individual patches is also visible. These patches are approximately 500–1000 nm in width and 5 nm in height. Sample [PM4.1 Fe_3O_4 FP] (Fig. 7(b)) had the highest concentration of any type of NPs added and shows features of 26.0 nm (± 6.4 nm) diameter across the surface, which may be attributed to aggregated Fe_3O_4 NPs. As shown by DLS and TEM (Fig. 2) the Fe_3O_4 NPs may aggregate to form clusters with size up to ~ 100 nm in diameter. The diameter of the circular features seems large initially when the AFM image is viewed from above and whilst the AFM image seems to show them as smooth, when the height profile is studied (Fig. 7(d), 2), individual NPs can be picked out at around 2.4 nm diameter. The large coverage of NPs in this image masks the PM underneath, indicating that the NPs added by facile penetration remained on the surface as the droplet evaporated rather than becoming intercalated in the PM multilayers. The d -spacing increase as discussed above, however, suggests that the aqueous medium must have permeated through the PM film, transporting ions with it. Further AFM images on the NP distribution on the PM film surface can be found in the ESI section.[†]

3.3. UV-Vis spectroscopy

In order to assess if the PM films retained their proton pumping ability after NP addition, UV-Vis spectroscopic measurements were performed on all the films (deposited on quartz) to see whether the retinal had retained its conformation (Figs. 8 and 9) as this is an indicator of whether the PM can still function as a proton pump. UV-Vis has been carried out previously on oriented PM films³¹ to assess the conformation of the retinal residue. As shown in Fig. 8 and 9, the UV-Vis spectrum of the control PM film shows a peak at the wavelength $\lambda \sim 560$ nm. In a study by Becher and Cassim,³² it was established that such an absorption peak was a signature for the transition of the retinal

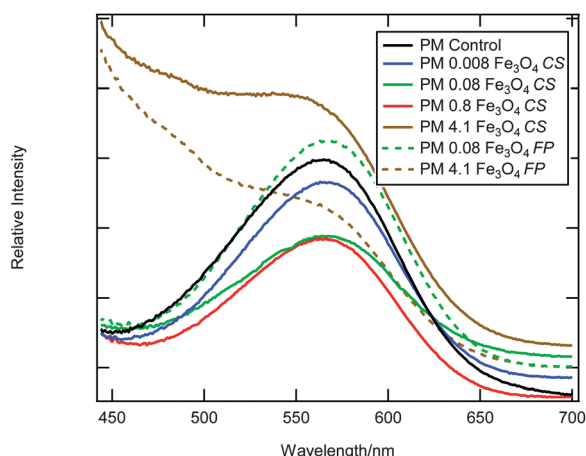


Fig. 8 UV-Vis spectra of PM control sample and PM films with Fe_3O_4 NPs added showing retention of function. All curves have the same shape except for the two with the highest concentration of magnetite [PM4.1 Fe_3O_4 CS] and [PM4.1 Fe_3O_4 FP] which whilst still exhibiting the peak for PM function, show additional absorption in the 450–540 nm wavelength range.

chromophore between two different energy levels upon exposure to light, designated as the $\pi-\pi^*$ (NV_1) transition. Thus, the presence of this peak in the UV-Vis spectrum indicates that because the retinal has retained its conformation the PM film should still be able to function as a proton pump. The results of whether this conformation has been retained are indicated in Table 1 in the experimental section. The UV-Vis spectra of all of the samples with NPs exhibited this peak, showing that the PM had most likely retained its proton pumping function after NP exposure in each case. The peak position differed slightly from that of the control (at 565 nm), and there was the most noticeable difference in peak position with the highest NP concentrations, with [PM0.2AuFP] (Fig. 9) having a peak position of 556 nm. Although the intensity of the absorption peak varies somewhat with the NP concentration, there is not a clear trend. The two samples with the highest concentration of Fe_3O_4 NPs ([PM4.1 Fe_3O_4 CS] and [PM4.1 Fe_3O_4 FP]) show a curve shape

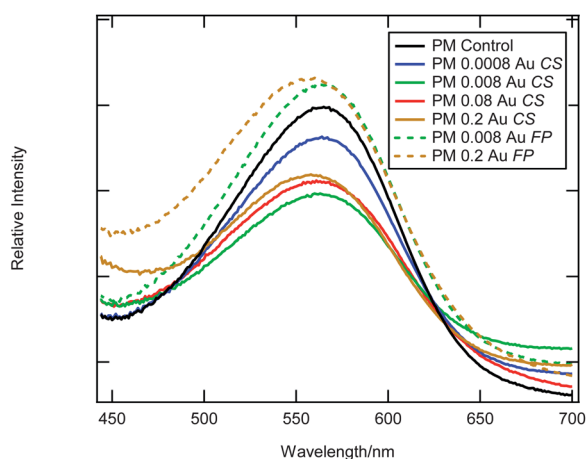


Fig. 9 UV-Vis spectra of PM control sample and PM films with AuNPs added showing retention of retinal conformation.

differing from all of the other samples, with a broad peak sloping from $\lambda \sim 450$ nm and merging with the $\lambda \sim 560$ nm peak. This is due to the high concentration of Fe_3O_4 NPs on the surface of the PM and such absorbance has been observed in both our Fe_3O_4 NPs control curve and in the literature.³³ The peak at $\lambda \sim 560$ nm remains visible indicating that the retinal residue has been unaffected.

3.4. Further discussion and concluding remarks

The overriding outcome of our results is that the NPs did not completely destroy the self-assembled multilayer structure of the PM films, and did not disrupt the conformation of retinal which is the chromophore in the bR protein responsible for its proton pumping function, for two NP addition methods investigated: attempted facial penetration (FP) by NPs of preformed PM films and adding NPs to PM aqueous solutions to attempt co-assembly (CS). Whilst in a previous study Collins *et al.*¹⁶ observed enhanced chemical and physical properties of PM films due to intercalation of polymer molecules, the NPs in our study did not enter the inter-lamellar space. Instead, AFM imaging has revealed that the NPs aggregated atop the PM films. However, despite the above, the effect of the NPs on the structure of the PM films is not completely inert. By examining the structural details of the PM multilayer stack, we have found that the thickness (*i.e.* the *d*-spacing) of the individual layers in the multilayer stack increased slightly with the increasing NP concentration. Concurrently, the correlation length *L*, which is a length scale related to the self-assembled domain size perpendicular to the stack, was found to decrease with the NP concentration. Collected together, these results indicate unequivocally that the number of layers in the multilayer stack decreased as more NPs were added. Previously, it has been pointed out that the stacking of PM would act to amplify the proton pumping effect. Thus, a reduction in the number of layers in the stack would compromise this property, and so the presence of NPs could have implications to the overall efficacy of the PM based devices.

Given that NPs did not intercalate in the inter-lamellar space, we have attributed the increase in *d* to possible binding of hydrated cations originating from NPs with amino acid residues on the bR proteins. This would result in increased fluidity and flexibility, leading to augmented undulation forces between the layers. The UV-Vis results show that the retinal chromophore's conformation remains intact, which is stabilised by an amino acid residue, Asp-212 (ref. 34) that also exposes a $-\text{COOH}$ terminus. We thus suggest that the hydrated cations originating from the NPs did not access the binding sites at the Asp-212. This interpretation of NPs not associating with the PM implies that the building units of PM films – bR and lipids – prefer to undergo self-assembly rather than affiliating with the NPs. This is probably due to the strong hydrophobic interaction between them that is the driving force for self-assembly in aqueous media, which overwhelms the competing binding forces between NPs and the amino acid residues. Once self-assembled, the rigidity of the PM patches would resist any bending curvature which would arise if the patches were to wrap around the NPs. The consideration of such bending elastic energy cost may also offer an explanation for NPs failure to invade the PM multilayers in the FP method of NP addition. Whilst NPs are known to infiltrate

lipid bilayers³⁵ and alter their structure, the bending modulus of the PM is much higher. The PM consists of 75% proteins and the bending modulus of its lipid–protein composite structure is ~ 8 MPa,³⁶ as compared to the lower moduli of a cell (*e.g.* 4–5 kPa for a fibroblast and 10–11 kPa for an endothelial cell).³⁷ This would lead to a much higher elastic energy cost if NPs were to enter the inter-lamellar space *via* a mechanism similar to the cellular entry by an NP. For similar arguments, in the CS process, the self-assembled PM is too rigid a structure to bend around the NPs, and prefers a low curvature. An alternative way of entering the inter-lamellar space would be to infiltrate through the edge. If that was the case, however, due to the rigidity of the PM, instead of being incorporated in the stack which would require bending of the PM, some of the PM layers would instead be cleaved off the stack, leading to a smaller coherence length and smaller number of layers in the lamellar structure as observed. Such considerations of elastic bending energy cost is also consistent with our postulation that hydrated cations may enter the inter-lamellar space and access amino acid residues, making the PM more fluid and flexible and leading to increased inter-layer repulsion and an increase in the *d*-spacing.

If we regard the PM patches as a self-assembled product and draw an analogy with the simpler and better defined micelle formation, then the shape and size of the self-assembled product is a result of the intricate balance between repulsion and attraction between self-assembling units, corresponding to an interaction free energy minimum. In general, conceptually, an increase in the repulsive force would lead to a decrease in the number of building units in the product. We thus may interpret the reduction in the number of the layers assembled in the multilayer stack as a result of increased inter-layer repulsion associated with the increasing NP concentration. A telling future experiment is to investigate NPs with hydrophobic surface chemistry, which would allow them to participate in the PM self-assembly process more readily and also encourage them to enter the hydrophobic cores of the PM layer. However, due to the fact that self-assembly of PM takes place in aqueous media and the PM is sensitive to organic solvents, the delivery of hydrophobic NPs would not be trivial.

Our results indicate that the effects of NPs on the structural integrity and functionality of PM films are complex. If we are to form PM–NP composites of desired geometry and dimension in order to exploit potential synergetic effects, the interactions between NPs and lipids/proteins that the PM comprises, as well as the elastic bending energy associated with forming these structures, should be considered.

Acknowledgements

We would like to thank T. Dane at the University of Bristol for his helpful comments on our manuscript, J. A. Jones at University of Bristol for his help with TEM imaging, and CRG Beamline BM28 at the European Synchrotron Radiation Facility (ESRF) for synchrotron beam time. J. Bulpitt is supported by a University of Bristol DTA studentship. WHB would like to acknowledge funding from the Engineering and Physical Science Research Council (EPSRC; EP/H034862/1), the University of Bristol, the Royal Society (UK) and the European Research Council (ERC).

Notes and references

- 1 L. Zhang, Y. H. Shen, A. J. Xie, S. K. Li and Y. M. Li, *J. Mater. Chem.*, 2009, **19**, 1884.
- 2 Y. Bar-Cohen, *Bioinspiration Biomimetics*, 2006, **1**, P1–P12.
- 3 C. Neinhuis and W. Barthlott, *Ann. Bot.*, 1997, **79**, 667.
- 4 T. A. Dickinson, J. White, J. S. Kauer and D. R. Walt, *Trends Biotechnol.*, 1998, **16**, 250–258.
- 5 R. Henderson, *Annu. Rev. Biophys. Bioeng.*, 1977, **6**, 87–109.
- 6 H. G. Khorana, G. E. Gerber, W. C. Herlihy, C. P. Gray, R. J. Anderegg, K. Nihei and K. Biemann, *Proc. Natl. Acad. Sci. U. S. A.*, 1979, **76**, 5046–5050.
- 7 R. A. Mathies, S. W. Lin, J. B. Ames and W. T. Pollard, *Annu. Rev. Biophys. Biophys. Chem.*, 1991, **20**, 491–518.
- 8 C.-W. Yen, L.-K. Chu and M. A. El-Sayed, *J. Am. Chem. Soc.*, 2010, **132**, 7250–7251.
- 9 J.-Y. Kim, S. Lee, K.-H. Yoo and D.-J. Jang, *Appl. Phys. Lett.*, 2009, **94**, 153301.
- 10 K. Sumitomo, Y. Shinozaki, D. Takagi, H. Nakashima, Y. Kobayashi and K. Torimitsu, *Jpn. J. Appl. Phys.*, 2009, **48**, 08JB18.
- 11 Y. H. Sun, J. R. Li, B. F. Li and L. Jiang, *Langmuir*, 1997, **13**, 5799–5801.
- 12 I. Ron, N. Friedman, M. Sheves and D. Cahen, *J. Phys. Chem. Lett.*, 2010, **1**, 3072–3077.
- 13 R. Li, X. Cui, W. Hu, Z. Lu and C. M. Li, *J. Colloid Interface Sci.*, 2010, **344**, 150–157.
- 14 K. M. Bromley, A. J. Patil, A. M. Seddon, P. Booth and S. Mann, *Adv. Mater.*, 2007, **19**, 2433–2438.
- 15 A. M. Collins, N. H. Mohd Kaus, F. Speranza, W. H. Briscoe, D. Rhinow, N. Hampp and S. Mann, *J. Mater. Chem.*, 2010, **20**, 9037.
- 16 A. M. Collins, D. Rhinow, N. Hampp and S. Mann, *Biomacromolecules*, 2009, **10**, 2767–2771.
- 17 J. Deschanvres, P. Rey and G. Delabouglise, *Sens. Actuators, A*, 1992, **33**, 43–45.
- 18 Y. Paz, Z. Luo, L. Rabenburg and A. Heller, *J. Mater. Res.*, 1995, **10**, 2842–2848.
- 19 G. Liu, R. Y. Hong, L. Guo, Y. G. Li and H. Z. Li, *Appl. Surf. Sci.*, 2011, **257**, 6711–6717.
- 20 M.-C. Daniel and D. Astruc, *Chem. Rev.*, 2004, **104**, 293–346.
- 21 Y.-Y. Kim, K. Hore, S. R. Hall and D. Walsh, *Small*, 2009, **5**, 913–918.
- 22 D. Walsh, Y.-Y. Kim, A. Miyamoto and F. C. Meldrum, *Small*, 2011, **7**, 2168–2172.
- 23 To estimate the number ratio ν of the NPs : PM trimers, firstly the number of PM trimers in each film was estimated. As each film was made up with 20 μL of a 5.5 mg mL⁻¹ solution of PM, the number of trimers in this volume was calculated as follows. The mass of the PM present in mg for each mL was converted into Daltons mL⁻¹, and this was then divided by the M_w of a PM trimer (78 000 Da) to work out the number of trimers in each mL, then divided by 50 to get the amount in each film (since 20 μL of the solution was used to form one film). As the PM film comprises 75 wt% bR and 25 wt% lipid, this amount was then multiplied by 0.75 to give an estimate of the number of PM trimers in each film. Knowing the mass of the NPs added to the PM film, the number of NPs in each film was estimated by working out the mass of an individual NP using the density of the bulk material. The number ratio was then calculated by dividing the number of NPs in a certain film by the number of bR trimers in that film.
- 24 To calculate the volume ratio, the density of the PM film, the lipid and the bR protein were all taken from the literature. The mass of one protein is 26 kDa or 4.32×10^{-17} mg. As the density of one protein (ρ_{pro}) is 1.28 g mL⁻¹ or 1280 mg mL⁻¹ (ref. 38), the volume of one protein can be calculated, then multiplied by three to give an approximate volume for each trimer of 1.01×10^{-19} cm³ or 1.01×10^{-25} m³.
- 25 I. Koltover, T. Salditt, J.-L. Rigaud and C. Safinya, *Phys. Rev. Lett.*, 1998, **81**, 2494–2497.
- 26 J. N. Israelachvili, *Intermolecular and Surface Forces: With Applications to Colloidal and Biological Systems*, Academic Press, 2nd edn, 1992.
- 27 T. Eliash, L. Weiner, M. Ottolenghi and M. Sheves, *Biophys. J.*, 2001, **81**, 1155–1162.

-
- 28 T. G. Dane, P. T. Cresswell, O. Bikondoa, G. E. Newby, T. Arnold, C. F. J. Faul and W. H. Briscoe, *Soft Matter*, 2012, **8**, 2824–2832.
- 29 A. Patterson, *Phys. Rev.*, 1939, **56**, 978–982.
- 30 D. L. Worcester, *J. Vac. Sci. Technol., A*, 1990, **8**, 403.
- 31 D. D. Muccio and J. Y. Cassim, *Biophys. J.*, 1979, **26**, 427–440.
- 32 B. Becher and J. Y. Cassim, *Biophys. J.*, 1976, **16**, 1183–1200.
- 33 R. Y. Hong, B. Feng, L. L. Chen, G. H. Liu, H. Z. Li, Y. Zheng and D. G. Wei, *Biochem. Eng. J.*, 2008, **42**, 290–300.
- 34 R. R. Birge, *Biochim. Biophys. Acta*, 1990, **1016**, 293–327.
- 35 B. Jing and Y. Zhu, *J. Am. Chem. Soc.*, 2011, **133**, 10983–10989.
- 36 A. Siitonen, K. Sumitomo, C. Ramanujan, Y. Shinozaki, N. Kasai, K. Furukawa, J. Ryan and K. Torimitsu, *Appl. Surf. Sci.*, 2008, **254**, 7877–7880.
- 37 B. J. Reynwar, G. Illya, V. A. Harmandaris, M. M. Müller, K. Kremer and M. Deserno, *Nature*, 2007, **447**, 461–464.
- 38 J. Marque, L. Eisenstein, E. Gratton, J. M. Sturtevant and C. J. Hardy, *Biophys. J.*, 1984, **46**, 567–572.